minerals

MDPI

Article

Trace Metal Distribution in Sulfide Minerals from Ultramafic-Hosted Hydrothermal Systems: Examples from the Kairei Vent Field, Central Indian Ridge

Yejian Wang [1,*], Xiqiu Han [1,*], Sven Petersen [2], Matthias Frische [2], Zhongyan Qiu [1], Yiyang Cai [1] and Peng Zhou [1,3]

1 Key Laboratory of Submarine Geosciences & Second Institute of Oceanography, State Oceanic Administration, Hangzhou 310012, China; qiuzy@sio.org.cn (Z.Q.); caiyiyang@sio.org.cn (Y.C.); pzhouklsg@sio.org.cn (P.Z.)
2 Helmholtz Centre for Ocean Research Kiel (GEOMAR), 24148 Kiel, Germany; spetersen@geomar.de (S.P.); mfrische@geomar.de (M.F.)
3 College of Marine Geosciences, Ocean University of China, Qingdao 266100, China
* Correspondence: yjwang@sio.org.cn (Y.W.); xqhan@sio.org.cn (X.H.)

Received: 4 September 2018; Accepted: 5 November 2018; Published: 11 November 2018

Abstract: The ultramafic-hosted Kairei vent field is located at 25°19′ S, 70°02′ E, towards the Northern end of segment 1 of the Central Indian Ridge (CIR-S1) at a water depth of ~2450 m. This study aims to investigate the distribution of trace elements among sulfide minerals of differing textures and to examine the possible factors controlling the trace element distribution in those minerals using LA-ICP-MS spot and line scan analyses. Our results show that there are distinct systematic differences in trace element distributions throughout the different minerals, as follows: (1) pyrite is divided into three types at Kairei, including early-stage euhedral pyrite (py-I), sub-euhedral pyrite (py-II), and colloform pyrite (py-III). Pyrite is generally enriched with Mo, Au, As, Tl, Mn, and U. Pyrite-I has high contents of Se, Te, Bi, and Ni when compared to the other types; py-II is enriched in Au relative to py-I and py-III, but poor in Ni; py-III is enriched in Mo, Pb, and U but is poor in Se, Te, Bi, and Au relative to py-I and py-II. Variations in the concentrations of Se, Te, and Bi in pyrite are most likely governed by the strong temperature gradient. There is generally a lower concentration of nickel than Co in pyrite, indicating that our samples precipitated at high temperatures, whereas the extreme Co enrichment is likely from a magmatic heat source combined with an influence of serpentinization reactions. (2) Chalcopyrite is characterized by high concentrations of Co, Se, and Te. The abundance of Se and Te in chalcopyrite over the other minerals is interpreted to have been caused by the high solubilities of Se and Te in the chalcopyrite lattice at high temperatures. The concentrations of Sb, As, and Au are relatively low in chalcopyrite from the Kairei vent field. (3) Sphalerite from Zn-rich chimneys is characterized by high concentrations of Sn, Co, Ga, Ge, Ag, Pb, Sb, As, and Cd, but is depleted in Se, Te, Bi, Mo, Au, Ni, Tl, Mn, Ba, V, and U in comparison with the other minerals. The high concentrations of Cd and Co are likely caused by the substitution of Cd^{2+} and Co^{2+} for Zn^{2+} in sphalerite. A high concentration of Pb accompanied by a high Ag concentration in sphalerite indicates that Ag occurs as Pb–Ag sulfosalts. Gold is generally low in sphalerite and strongly correlates with Pb, suggesting its presence in microinclusions of galena. The strong correlation of As with Ge in sphalerite from Kairei suggests that they might precipitate at medium temperatures and under moderately reduced conditions. (4) Bornite–digenite has very low concentrations of most trace elements, except for Co, Se, and Bi. Serpentinization in ultramafic-hosted hydrothermal systems might play an important role in Au enrichment in pyrite with low As contents. Compared to felsic-hosted seafloor massive sulfide deposits, sulfide minerals from ultramafic-hosted deposits show higher concentrations of Se and Te, but lower As, Sb, and Au concentrations, the latter often attributed to the contribution of magmatic volatiles. As with typical ultramafic-hosted seafloor

massive sulfide deposits, Se enrichment in chalcopyrite from Kairei indicates that the primary factor that controls the Se enrichment is temperature-controlled mobility in vent fluids.

Keywords: trace elements; hydrothermal sulfides; Laser Ablation ICP-MS; ultramafic-hosted; Central Indian Ridge

1. Introduction

Seafloor massive sulfide (SMS) deposits occur at mid-ocean ridges and also in submarine volcanic arcs and related back-arc basins associated with host rocks of highly variable composition [1]. The geochemical composition of SMS is also highly variable. For example, sulfide minerals from basalt-hosted mid-ocean ridges appear to be depleted in Au, Ag, As, Sb, and Pb compared to sulfide minerals from hydrothermal systems in back-arc basins (e.g., [1,2]). Additionally, sulfide minerals from occurrences associated with ultramafic host rocks at mid-ocean ridges have significantly higher average Au and Cu contents, when compared to the basalt-hosted deposits (e.g., [3–5]). Hence, the geodynamic settings of seafloor hydrothermal systems with their variable host rock compositions represent a first-order control on the geochemical composition of SMS deposits [6].

Sulfide precipitation from hydrothermal fluids that transport metals leached from the host rock, is governed by physico-chemical parameters, such as temperature, salinity, pH, and fO_2-fS_2. Processes such as cooling, boiling, mixing, and fluid–rock interactions are key for sulfide precipitation in hydrothermal systems, as they can influence the main parameters above [7–9]. Previous studies suggest that the recognition of distinct trace element signatures of individual sulfide grains from seafloor hydrothermal systems can assist with tracking sequences of crystallization and stages of mineralization, sources of metals, and evolution of ore-forming fluids over time in SMS deposits (e.g., [10–12]). Recent work by Wohlgemuth-Ueberwasser et al. (2015) [13], Keith et al. (2016) [8], Melekestseva et al. (2017) [14], and Wang et al. (2017) [15] investigated trace element distributions using laser ablation ICP-MS analysis in sulfide minerals from SMS deposits in different geodynamic settings including ultramafic-hosted and basalt-hosted fields as well as a number of fields that are associated with submarine volcanic arcs and back-arc basins. Those studies demonstrated that all of the parameters mentioned above influence geochemistry and mineralogy and may account for the variable metal enrichment of SMS. There is comparably little data in hydrothermal fields from the Indian Ocean. A recent publication [4] focused on the mineralogy and bulk geochemistry of massive sulfides from the Kairei vent field on the Central Indian Ridge and suggested that the enrichment of Cu, Zn, and trace elements, such as Au, Co, and Sn, is related to the involvement of ultramafic rocks in the subseafloor, thereby strengthening earlier observations from fluid chemistry (hydrogen and methane enrichment) and petrology (sampling of ultramafic rocks to the east of the active vent field). High-resolution geochemical analyses on sulfide minerals have only been conducted for a few ultramafic-hosted SMS deposits at mid-ocean ridges. For the Kairei vent field, LA-ICP-MS analyses have been performed on pyrite [8], but there is still little known about the incorporation mechanism of trace elements that are normally enriched in the ultramafic-hosted SMS deposits (e.g., Co, Ni, Sn) in sphalerite and Cu–(Fe)–sulfides.

In the present work, we therefore analyze the major sulfide minerals from the Kairei vent field that come from a wide range of sample types (chimney, massive sulfides, and breccias) for trace elements using LA-ICP-MS spot analyses and line scans. This study aims to investigate the distribution of trace elements among sulfide minerals of differing textures, such as pyrite, chalcopyrite, sphalerite, bornite, and covellite, and examine the possible contributing factors (e.g., formation temperature, seawater–fluid mixture, redox) controlling the trace element distribution in these minerals.

2. Geological Background

The Kairei vent field is located at 25°19′ S, 70°02′ E, towards the Northern end of segment 1 of the Central Indian Ridge (CIR-S1), at a water depth of ~2450 m (Figure 1; [16]). Kairei occurs ~1800 m above the rift valley floor on its Eastern wall and is situated over 7 km away from the axial volcanic ridge. The rift valley wall has a stair-step morphology in this region and the active vent field occurs on the Western flank of Hakuho Knoll within a larger area of massive sulfides (Figure 1b; [17,18]). The discharging fluids at the vent field reach temperatures of 365 °C and are characterized by high concentrations of H_2 and CH_4 [17,19], which is comparable to ultramafic-hosted hydrothermal fields along the Mid-Atlantic Ridge (e.g., [20–24]). The outcrops in the vicinity of the vent field are entirely made up of pillow basalt and sheet flows, and no exposures of ultramafic rocks were observed [17–19]. However, two oceanic core complexes (Uraniwa Hills and Yokoniwa Rise; Figure 1b) consisting of peridotitic and gabbroic rocks have been identified within ~15 km of Kairei [25,26]. Another large core complex has been documented on the Western slopes of the CIR in this area [27]. It was suggested that the combination of the troctolite alteration at the recharge zone near the oceanic core complex and subsequent basalt alteration at the discharge zone under Kairei is causing the distinct chemistry of the vent fluids [18,25]. Recent investigations have shown the presence of other ultramafic-hosted massive sulfide deposits (e.g., the Yokoniwa vent field) in the area [26].

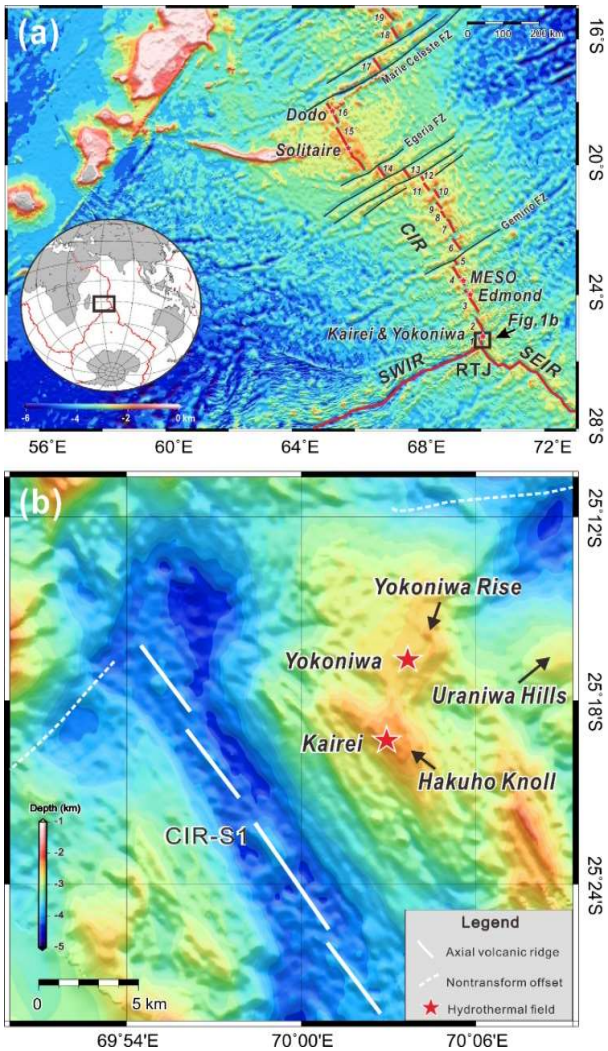

Figure 1. (**a**) Geological map of the Central Indian Ridge (CIR) and (**b**) location of the Kairei vent field. Other known hydrothermal fields are indicated by red stars. Note, segment numbering is from Okino et al. (2015) [28]. SWIR = Southwest Indian Ridge; SEIR = Southeast Indian Ridge. Bathymetry data source: Global Multi-Resolution Topography (GMRT) synthesis [29].

The main mineralogical characteristics (Figure 2) of Zn-rich chimney and massive sulfide samples from the Kairei vent field were described in Wang et al. (2012, 2014) [4,30]. Three mineralization stages were identified at this site: (1) a high temperature stage consisting largely of chalcopyrite, isocubanite, and pyrite; (2) a medium to low temperature stage characterized by the mineral assemblages of sphalerite and pyrite; and (3) a late stage of waning hydrothermal activity and weathering characterized by secondary Cu–(Fe)–sulfides (bornite, digenite, covellite, and idaite), Fe–oxyhydroxides, opal-A, and Cu–chloride (paratacamite and atacamite) were related to the increasing influence of oxygenated seawater. The observed Cu–(Fe)–sulfide sequence of isocubanite → chalcopyrite → bornite (including bornite–digenite intergrowths) → minerals of the Cu–S system (covellite–idaite solid solutions) exists along a path of increasing oxidation and sulfidation state and is common at Kairei. Dating ($^{230}Th/^{234}U$) of massive sulfides collected from Kairei shows ages ranging from 8.4 to 96.3 ka [30], indicating a prolonged hydrothermal history at this site.

3. Samples and Methods

The samples from Kairei are Zn-rich chimneys, Cu-rich massive sulfides, and sulfide-bearing breccias that were recovered using a TV-grab during R/V Dayangyihao DY17A and DY19III cruises in 2005 and 2007 (Table 1). In advance of the laser-ablation analyses, eight thin, polished sections were examined microscopically in order to identify the different mineral phases (Figure 2) and to avoid measuring grains with visible mineral inclusions. A total of 99 representative analyses were performed by electron microprobe for major element composition [4], and on these samples, 64 points were analyzed by laser ablation ICP-MS.

The laser ablation ICP-MS study was performed with a 193 nm ArF excimer laser ablation system (GeoLasPro, Coherent) coupled to a double-focusing, high-resolution magnetic sector mass spectrometer (Nu Instruments, AttoM) in low resolution mode (300 Res, 10% valley definition) at the GEOMAR Helmholtz Center for Ocean Research Kiel, Germany. Sample ablation was performed under He carrier gas with Ar transport gas added after the ablation cell. Spot analysis on sulfide minerals was done by 30 s of ablation at a laser repetition rate of 5 Hz, a beam diameter of 44 µm, and a fluence of 2 J cm^{-2}. Forty seconds of gas background was collected prior to each ablation. A NIST SRM610 glass standard (30 s, 10 Hz, 32 µm, 5 J·cm^{-2}; [31]) was used for calibration. Additionally, a synthetic sulfide reference standard material (trans_1; 30 s, 5 Hz, 44 µm, 2 J·cm^{-2}; [32]) was used to calibrate sulfur (39.1 ± 0.1 wt % S; Wohlgemuth-Ueberwasser pers. comm.). MPI-DING glasses (ATHO-G, GOR132-G, KL2-G; 30 s, 10 Hz, 44 µm, 5 J·cm^{-2}; [33]) and trans_1 were used as reference materials (results are presented in Table S1). Gas flows, torch position, and ion-optics-focusing were optimized to provide a maximum in ion transmission and low polyatomic cluster production rate ($ThO/Th \leq 0.03\%$; $CuAr/Cu < 0.0025\%$) by hot plasma (normalized argon index (NAI) ≈ 30; [34]) and a fast sample wash-out. The following isotopes were monitored by the analytical routine: ^{24}Mg, ^{29}Si, ^{51}V, ^{55}Mn, ^{57}Fe, ^{59}Co, ^{60}Ni, ^{63}Cu, ^{66}Zn, ^{71}Ga, ^{73}Ge, ^{75}As, ^{77}Se, ^{95}Mo, ^{107}Ag, ^{111}Cd, ^{115}In, ^{118}Sn, ^{121}Sb, ^{128}Te, ^{135}Ba, ^{197}Au, ^{205}Tl, ^{208}Pb, ^{209}Bi, and ^{238}U. Data evaluation of element concentrations was carried out using the linear slope regression method [35].

Table 1. Coordinates of sampling stations and mineral abundances of the sulfides from the Kairei vent field.

Sampling Station	Longitude (E)	Latitude (S)	Depth (m)	Type of Samples	Mineral Assemblage
17A-TVG7-1	70°02.408′	25°19.252′	2430	Cu-rich massive sulfides	cpy+bn+dg+py+(sph+iso+cv+id)
17A-TVG7-3	70°02.408′	25°19.252′	2430	Breccias	q+opal-A+tl+sph+py
17A-TVG9	70°02.420′	25°19.221′	2437	Zn-rich chimney	sph+py+mar+cpy
19III-TVG6	70°02.440′	25°19.230′	2443	Cu-rich massive sulfides	cpy+dg+bn+cv+py+iso+id
19III-TVG7	70°02.410′	25°19.220′	2440	Cu-rich massive sulfides	cpy+dg+bn+cv+py+id

Note: cpy—chalcopyrite, bn—bornite, dg—digenite, py—pyrite, sph—sphalerite, cv—covellite, id—idaite, iso—isocubanite, mar—marcasite, q—quartz, tl—tal.

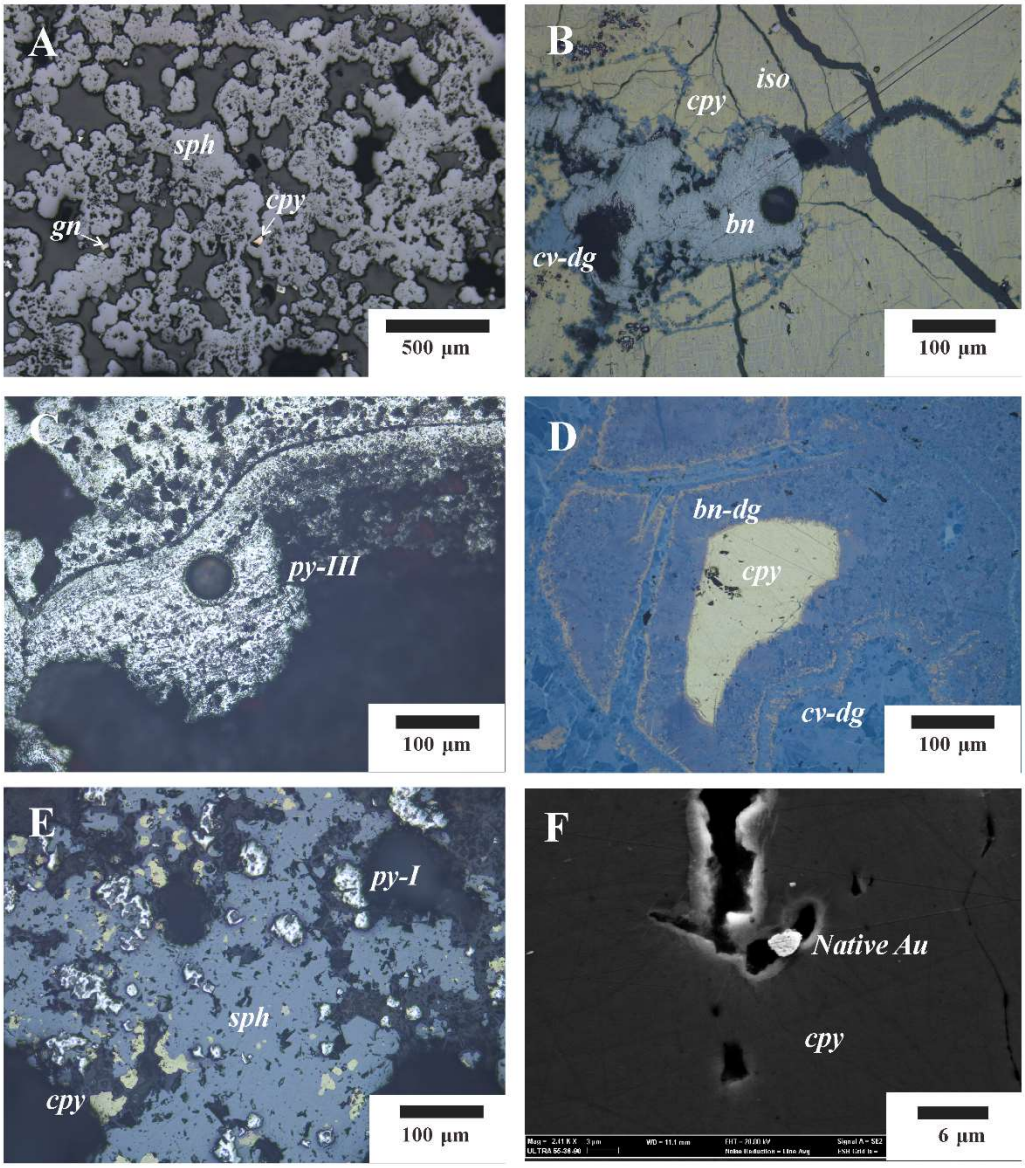

Figure 2. Optical and SEM photomicrographs of typical mineral assemblages. (**A**) colloform sphalerite and galena grains in the Zn-rich chimney sulfides (sample 17A-TVG9); (**B**) massive chalcopyrite intensely intergrown with isocubanite and surrounded by bornite and covellite–digenite intergrowths (sample 17A-TVG7-1D); (**C**) colloform pyrite in outlier of the Zn-rich chimney sulfides (sample 17A-TVG9); (**D**) bornite–digenite and covellite–digenite intergrowth surrounding chalcopyrite (sample 19III-TVG6); (**E**) massive sphalerite and co-genetic chalcopyrite and euhedral pyrite (sample 17A-TVG9); (**F**) native gold particles associated with chalcopyrite (sample 17A-TVG7-1D). Abbreviations: bn–dg = bornite–digenite intergrowths, cpy = chalcopyrite, cv–dg = covellite–digenite intergrowths, py = pyrite, sph = sphalerite.

4. Results

Full details of the LA-ICP-MS dataset are given in Table S2, including the concentration, analytical precision, and minimum detection limits for each element. The average concentrations of trace elements were calculated for the different sulfide minerals and morphologies (Table 2). Representative time-resolved LA-ICP-MS depth profiles are shown in Figure 3 for pyrite, chalcopyrite, sphalerite, bornite–digenite, and covellite–digenite. Figure 4 shows the trace element distribution in different sulfide mineral phases. In addition, line scan analysis of the pyrite in the Zn-rich chimney sample (17A-TVG9) was carried out, and the resulting mass spectrum is shown in Figure 5.

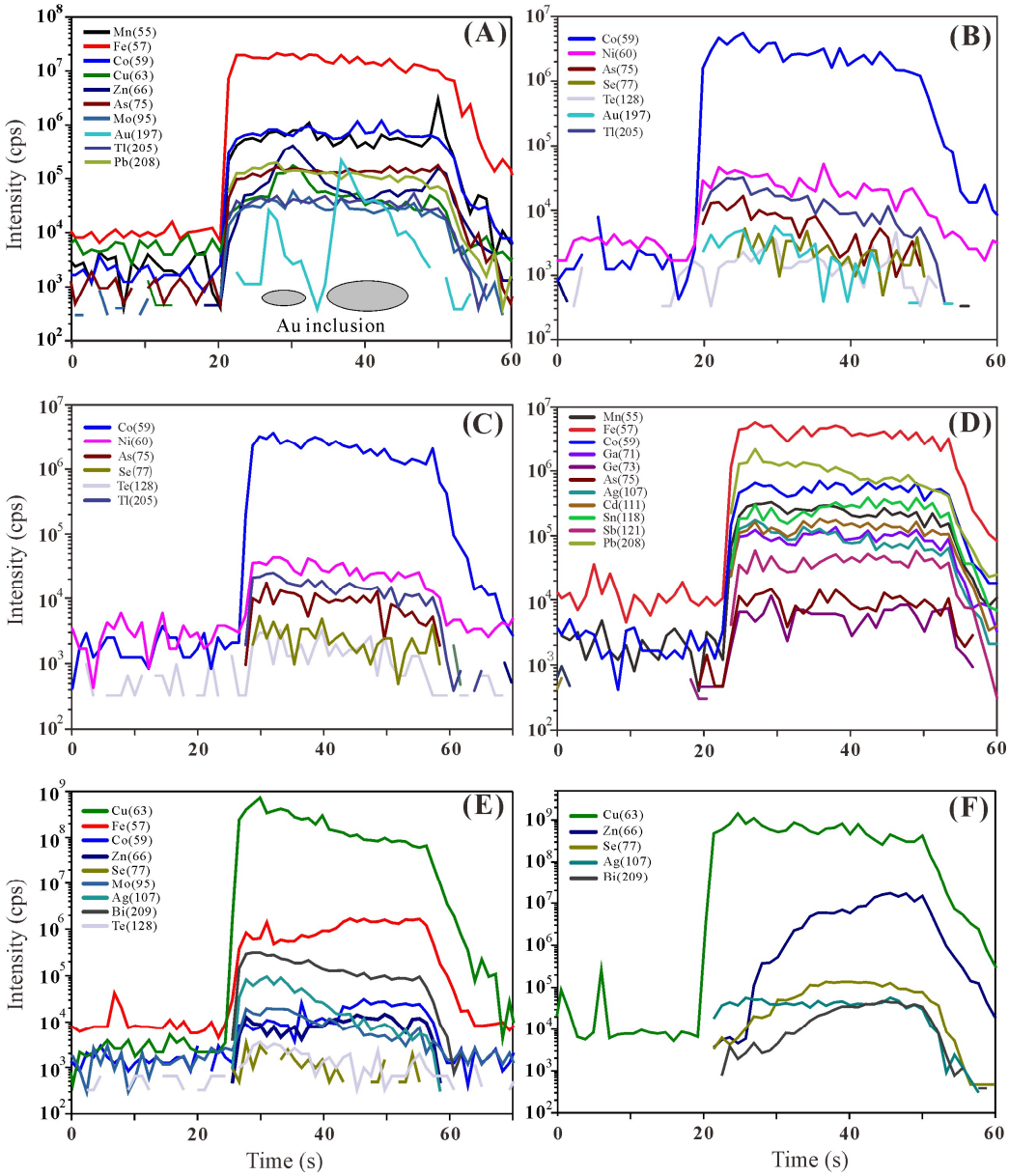

Figure 3. Representative time-resolved LA-ICP-MS depth profiles of selected elements in sulfide minerals from the Kairei vent field. (**A**) subhedral pyrite in Zn-rich chimney sulfides with inclusions of native gold; (**B**) chalcopyrite in the Cu-rich massive sulfide samples shows a homogeneous distribution of Ni, As, and Tl; (**C**) chalcopyrite showing a homogeneous distribution of Co, As, Mo, and Pb; (**D**) sphalerite with co-varying amounts of Fe and Co, Ag, Ga, Sn, and Mn; (**E**) early bornite with homogeneous Bi, Co, Mo, Ag, and Te distribution indicated by the flat signal intensities; (**F**) early bornite with elevated Zn, Bi, and Se.

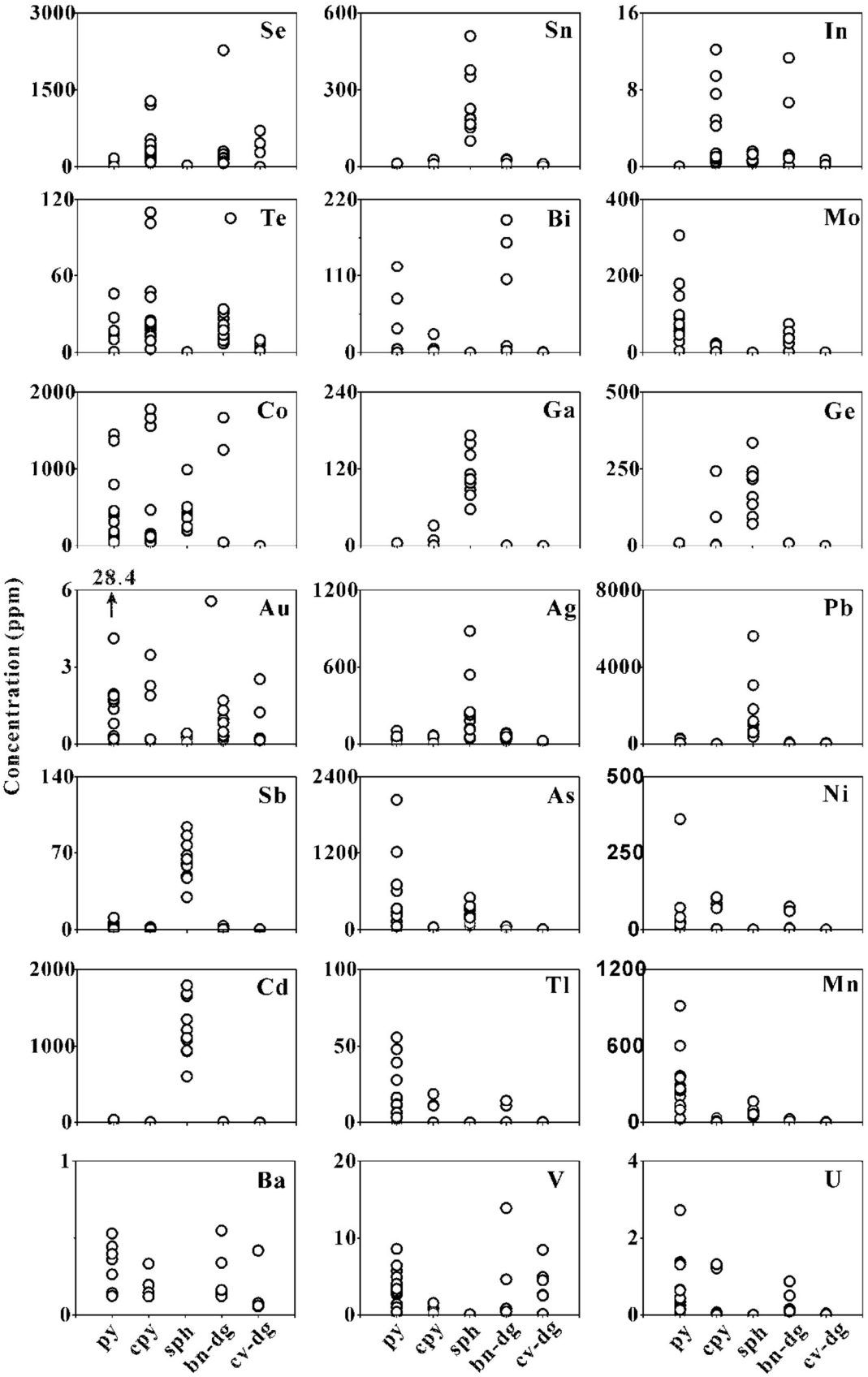

Figure 4. Distribution of trace elements in sulfide minerals from the Kairei vent field. Abbreviations: bn–dg = bornite–digenite intergrowths, cpy = chalcopyrite, cv–dg = covellite–digenite intergrowths, py = pyrite, sph = sphalerite.

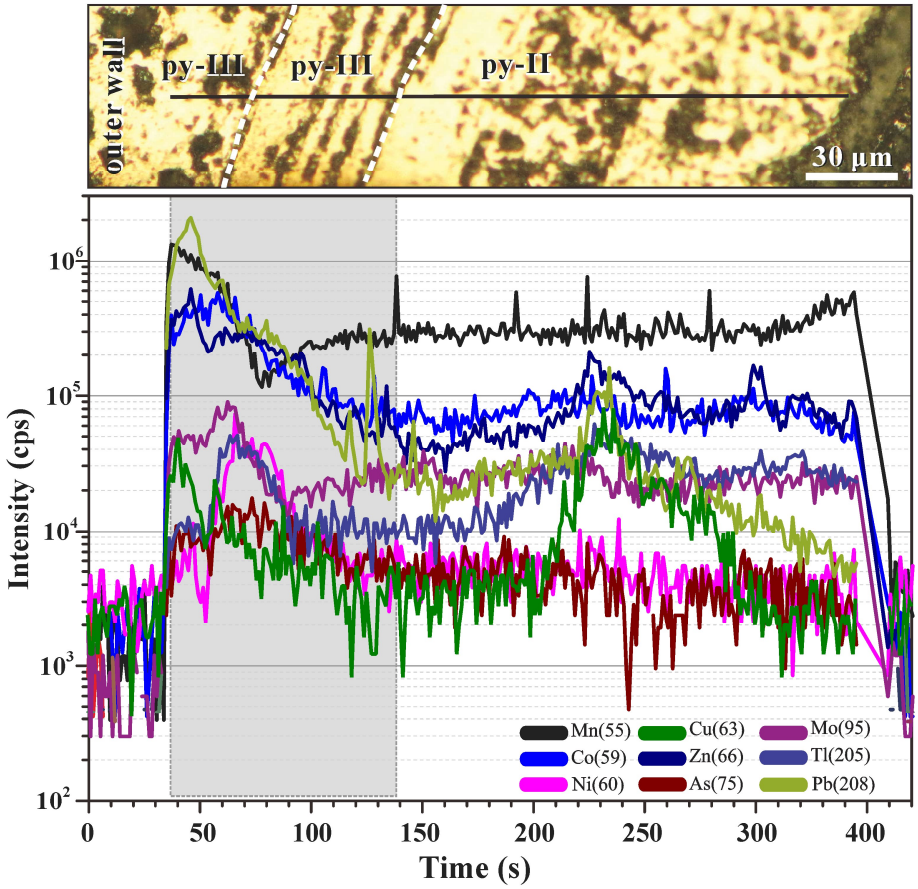

Figure 5. Signal sequence of a line scan analysis of colloform pyrite III and subhedral pyrite II in sample 17A-TVG9. The mass spectrum of colloform pyrite III is marked by high trace element concentrations (Mn, Pb, Cu, Zn, Co, and Mo) that generally decrease towards the more homogeneous subhedral pyrite II.

4.1. Pyrite

A total of nineteen spot analyses was completed on pyrites selected from different samples of the Kairei vent field, including eight euhedral pyrites (py-I), five subhedral pyrites (py-II), and six colloform pyrites (py-III). Pyrite is generally enriched in Mo, As, Tl, Mn, and U compared to the other investigated sulfide minerals (Figure 4, Table 2). Pyrite with different textures showed distinct variations in the trace element contents (Figures 5 and 6, Table 2). Compared to the other textural types, euhedral py-I tended to have higher contents of Se (up to 168 ppm; average: 65.3 ppm), Ni (up to 363 ppm; average: 51.4 ppm), Bi (up to 123 ppm; average: 30.4 ppm), and Te (up to 46.0 ppm; average: 14.3 ppm), when compared to py-II and py-III. Colloform py-III had distinctly higher concentrations of Mo (46–307 ppm; average:136 ppm), Pb (14–295 ppm; average: 105 ppm), and U (up to 2.73 ppm; average: 0.90 ppm) but was poor in Se, Te, Bi, and Au. Subhedral py-II was poor in most trace elements, but one single spot showed abnormally high Au concentrations (28.4 ppm; Table S2). However, enrichments of As (up to 2041 ppm) and Co (up to 1453 ppm) were common in all generations of pyrites. Py-I contained 395 ppm Co and 135 ppm As, on average; py-II had average As and Co concentrations of 254 ppm and 230 ppm, respectively; while py-III was characterized by concentrations of 614 ppm As and 466 ppm Co, on average.

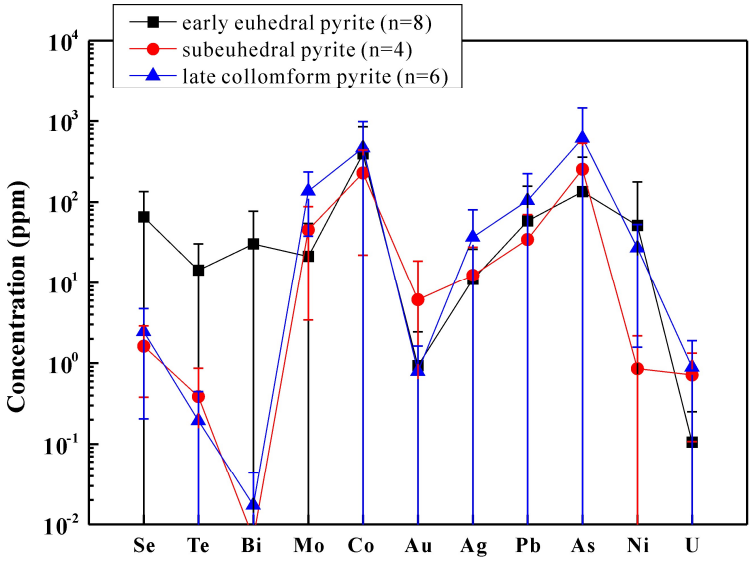

Figure 6. Average trace element concentrations in different pyrite types of the Kairei vent field.

A line scan analysis in chimney sample 17A-TVG9 conducted across a boundary between colloform py-III and subhedral pyrite II (Figure 5) exemplified the differences. The ablation of colloform py-III was marked by high trace element concentrations (Mn, Pb, Cu, Zn, Co, and Mo) that generally decreased towards the more homogeneous subhedral py-II.

4.2. Chalcopyrite

Sixteen chalcopyrite grains were analyzed in samples from the Kairei vent field. The chalcopyrite samples were characterized by high concentrations of Co (32–1781 ppm; average: 445 ppm), Se (62–1283 ppm; average: 363 ppm), and Te (up to 110 ppm; average: 29.7 ppm). The mean concentrations of Mo, Ag, Pb, Sb, As, Cd, and Mn were generally lower than in the other sulfide minerals; however, single measurements with enrichments in Zn (1740 ppm), Ge (243 ppm), and Au (3.5 ppm) did occur (Figure 4, Table S2).

4.3. Sphalerite

Sphalerite (n = 10) from Zn-rich chimneys was characterized by higher concentrations of Pb (363–5616 ppm), Cd (609–1792 ppm), Co (196–993 ppm), As (60.7–502 ppm), Ag (43.7–882 ppm), Sn (101–510 ppm), Ge (72.2–336 ppm), Ga (57.1–173 ppm), and Sb (29.7–94.2 ppm) relative to the other minerals. Sphalerite had depleted in Se, Te, Bi, Mo, Au, Ni, Tl, Mn, Ba, V, and U when compared to the other sulfide minerals (Figure 4, Table 2).

4.4. Bornite–Digenite Assemblage

Ten measurements were performed on bornite–digenite intergrowths in the Cu-rich sulfide samples. The results given in Table 2 indicate that bornite–digenite intergrowths were depleted in most trace elements when compared to the other sulfide minerals, except for Se (70.3–2272 ppm), Co (0.02–1669 ppm), and Bi (<0.001 ppm–191 ppm). Interestingly, the highest concentrations of Se (up to 2272 ppm) and Bi (up to 191 ppm) in all the sulfide minerals were observed in a bornite–digenite grain.

4.5. Digenite–Covellite Assemblage

Digenite–covellite intergrowths (n = 9) from the Cu-rich massive sulfide samples were characterized by generally low trace element concentrations (Figure 4, Table 2). Exceptions were Se (up to 702 ppm), Ag (up to 28.3 ppm), and 2.9 ppm Au on a single spot.

5. Discussion and Conclusions

5.1. Controls on Trace Elements in Pyrite

Pyrite is the most common sulfide mineral in hydrothermal ores and large mineral chemical data sets exist for SMS deposits over a wide range of geodynamic settings, including mid-ocean ridges, submarine volcanic arcs, and related back-arc basins (e.g., [6,8,13,15,36–38]). Previous studies have shown that most trace elements in pyrite likely reside in microinclusions of different grains, except for Cu, Co, Ni, Se, and As, which commonly occur in solid solution and result from Fe or S substitution [8,39].

Colloform pyrite (py-III) in the Zn-rich chimneys was consistently enriched with Pb, Mo, As, and U (Figure 6) relative to the other pyrite varieties. Euhedral pyrite (py-I), which is a main constituent of both sulfide-bearing breccia and Zn-rich chimneys, had high concentrations of Se, Te, Ni, Bi, and Au when compared to the colloform py-III but was depleted in Mo and U. Enrichments of As (mean 376 ppm) were common in all generations of pyrites at the Kairei vent field, and a positive correlation was observed between As and Ag (R^2 = 0.74). This could indicate co-incorporation of the two elements resulting from As^{3+} and Ag^{+} coupled substitution for $2Fe^{2+}$ [40,41]. Variations in the concentrations of Se (<0.04 to 168 ppm), Te (<0.05 to 46.0 ppm), and Bi (<0.02 to 123 ppm) in pyrite are likely governed by the strong temperature gradient [41]. Nickel concentrations (<0.04 to 363 ppm) were generally lower than those for Co in pyrite (Co/Ni = 3–172 ppm), indicating that the investigated samples precipitated under high temperature conditions [e.g., [42,43]]. Similar enrichments of Co in pyrite have been described from sulfides sampled at the Mid-Atlantic Ridge 5°S vent field with an average of 602 ppm (Table 3; [8]). Previous studies have shown that the Co is concentrated in high temperature fluids and is highly sensitive to changes in fluid temperature [44,45]. The high exit temperature for black smoker fluids at the Kairei vent field (up to 365 °C; [19]) indicates little or no interaction with seawater during upwelling. In addition, the results of Gallant and Von Damm (2006) [19] indicate that diking may be a mechanism for the heat source of the Kairei vent field. Hence, the Co enrichment in pyrite at Kairei might be related to a phase of recent magmatic activity [8]. However, besides pyrite, chalcopyrite and sphalerite at Kairei also have higher Co contents compared to minerals from the mafic-hosted Wocan vent field at the Carlsberg Ridge (Table 3; see discussion below). The Co-enrichment in all sulfide minerals at Kairei may therefore also point to an ultramafic influence at this site. Higher contents of Au (up to 28.4 ppm) are most likely related to inclusions of native gold which were observed in a single grain (Figure 3A), which is similar to observations by Keith et al. (2016) [8]. Uranium, which is normally derived from seawater, is also enriched in colloform pyrite compared to the other pyrite textures. This U enrichment is commonly observed in SMS deposits (e.g., [10,15,42]).

Table 2. Average trace element concentrations from LA-ICP-MS for the sulfides of the Kairei vent field.

Mineral	ppm (*n*)	Se	Sn	Te	Bi	Mo	Co	Ga	Ge	Au	Ag	Pb	Sb	As	Ni	Cd	Tl	Mn	U
py all	avg.(*19*)	28.7	1.54	6.19	12.8	64.0	374	0.50	1.97	2.26	19.5	66.7	1.79	318	30.5	5.44	13.5	213	0.52
	SD	53.6	3.15	12.3	32.7	78.4	416	1.17	2.81	6.42	28.5	93.7	2.71	525	82.5	8.73	17.2	235	0.71
py-I	avg.(*8*)	65.3	1.37	14.3	30.4	21.4	395	0.47	1.92	0.93	11.0	58.4	0.72	135	51.4	4.08	5.52	64.1	0.11
	SD	68.8	2.24	16.1	46.3	33.2	452	0.94	2.71	1.50	15.1	98.3	1.06	224	126	7.87	7.65	102	0.14
py-II	avg.(*5*)	1.63	0.57	0.39	0.01	45.7	230	0.24	1.73	6.13	12.4	34.6	1.41	254	0.86	2.27	27.2	387	0.72
	SD	1.25	0.59	0.48	0.01	42.2	208	0.41	1.94	12.5	15.1	35.4	1.18	277	1.32	1.84	25.1	311	0.61
py-III	avg.(*6*)	2.47	2.57	0.20	0.02	136	466	0.76	2.24	0.79	36.8	105	3.53	614	27.2	9.88	12.7	266	0.90
	SD	2.26	5.11	0.25	0.03	98.3	520	1.80	3.88	0.84	43.5	119	4.26	836	25.6	12.2	13.7	193	0.99
cpy	avg.(*16*)	363	10.2	29.7	2.77	4.08	445	3.05	22.8	0.50	14.0	4.7	0.31	8.6	23.3	3.61	2.61	11.2	0.25
	SD	369	7.3	32.5	6.44	8.0	621	8.07	63.2	1.06	22.7	9.4	0.62	17.8	40.9	2.74	5.84	11.9	0.50
sph	avg.(*10*)	21.3	248	0.26	0.05	b.d.l.	423	112	179	0.12	264	1529	63.4	267		1237	0.06	80.2	b.d.l.
	SD	3.04	126	0.27	0.04		229	36.3	86.3	0.14	259	1657	19.2	137		381	0.12	34.2	
bn–dg	avg.(*10*)	372	11.3	19.2	47.1	23.4	301	0.49	1.66	0.64	52.0	23.8	0.74	16.9	14.7	3.27	2.63	13.4	0.19
	SD	671	9.55	9.19	74.8	26.8	619	0.36	2.68	0.54	23.3	32.1	1.01	23.3	28.2	3.77	5.46	10.1	0.28
cv–dg	avg.(*9*)	211	1.94	2.53	0.24	b.d.l.	0.33	0.29	0.09	0.49	14.92	6.6	0.09	1.12	0.16	0.99	0.02	2.62	0.01
	SD	260	3.61	3.51	0.48		0.37	0.29	0.21	0.81	10.51	14.5	0.15	2.74	0.42	1.70	0.04	3.18	0.02

Note: Avg.= average content of trace element; SD = standard deviation of the average (1δ); *n* = number of analyses; b.d.l = below the minimum detection limit.

Table 3. Average contents (ppm) of selected trace elements in the sulfide minerals in the seafloor hydrothermal systems.

Region	Vent Field	Hosted Rock	Minerals	*n*	Co	Ni	As	Se	Sb	Te	Au	Source *
Central Indian Ridge	Kairei	Ultramafic	py	*19*	374	30.5	318	28.7	1.79	6.19	2.26	1
	Kairei	Ultramafic	cpy	*16*	445	23.3	8.6	363	0.31	29.7	0.50	1
	Kairei	Ultramafic	sph	*10*	423		267	21.3	63.4	0.26	0.12	1
	Kairei	Ultramafic	bn-dg	*10*	301	14.7	16.9	372	1.06	19.2	0.64	1
	Kairei	Ultramafic	cv-dg	*9*	0.33	0.16	1.12	211	0.09	2.52	0.49	1
	Kairei	Ultramafic	py	*39*	279	22.2	179	9.49	1.89		2.31	2
	MESO	Basaltic	py	*77*	392	1.41	909	745	9.21		0.89	2
Carlsberg Ridge	Wocan	Basaltic	py	*19*	110	11.8	224	36.4	3.91	1.40	0.43	3
	Wocan	Basaltic	dg	*11*	0.09	1.51	16.6	0.90	2.96	0.10	0.56	3
	Wocan	Basaltic	bn	*11*	0.11	0.30	0.67	2.54	5.17	0.24	0.36	3
	Wocan	Basaltic	sph	*17*	0.06	0.15	726	0.37	86.0	0.20	0.42	3
	Wocan	Basaltic	cpy	*22*	0.11	0.41	235	52.4	23.0	0.88	0.49	3

Table 3. *Cont.*

Region	Vent Field	Hosted Rock	Minerals	*n*	Co	Ni	As	Se	Sb	Te	Au	Source *
Mid-Atlantic Ridge	Logatchev	Ultramafic	py	*34*	102	19.3	47.2	9.56	12.2		1.23	2
	Logatchev	Ultramafic	cc	*15*			42.5	87.9	17.8	4.40	4.92	4
	Logatchev	Ultramafic	cpy	*29*			92.4	119	22.0	39.2	3.12	4
	Logatchev	Ultramafic	cc-cv	*12*			6.75	bdl	1.38	7.30	0.55	4
	Logatchev	Ultramafic	py	*23*			326	15.5	11.2	0.58	4.18	4
	Logatchev	Ultramafic	sph	*10*			214	1.68	233	0.73	3.73	4
	Semeynov-1	Ultramafic	py	*21*	2.07	0.81	510	9.20		0.51	33.1	5
	Semeynov-2	Ultramafic	cpy	*5*	340	13.0	1144	288	25.0	42.0	0.15	6
	Semeynov-2	Ultramafic	sph-wurt	*6*	84.0	0.20	424	129	214	8.51	3.00	6
	Semeynov-2	Ultramafic	cv-A	*8*	21.0	3.00	421	1024	579	97.0	173	6
	Semeynov-2	Ultramafic	cv-B	*3*	9.00	1.00	82.0	222	81.0	48.0	72.0	6
	Turtle Pits	Basaltic	cpy	*15*			37.9	204	0.46	4.73	0.06	4
	Turtle Pits	Basaltic	py	*40*			224	25.2	4.94	1.20	0.25	4
	Turtle Pits	Basaltic	sph	*20*			147	28.2	47.9	0.62	0.36	4
	TAG	Basaltic	py	*61*	269	2.28	60.9	43.4	1.55		0.23	2
	5°S	Basaltic	py	*34*	602	1.12	742	30.1	4.57		0.33	2
Valu Fa Ridge	Hine Hina	Basaltic–andesitic	py	*65*	144	16.0	33.2	26.5	1.50		0.61	2
Okinawa Though	Jade	Basaltic–rhyolitic	py	*39*	2.22	2.84	688	44.9	18.0		0.73	2
Kermadec Arc	Brothers	Dacitic	py	*77*	210	2.42	896	481	2.97		0.36	2
Tonga Arc	Volcano 19 (cone)	Basaltic-basaltic andesitic	py	*114*	16.1	1.13	9100	11.0	34.3		12.2	2
	Volcano 19 (caldera)	Basaltic-basaltic andesitic	py	*76*	0.80	3.01	10240		623		1.55	2
Manus Basin	PacManus-RR	Basaltic–rhyolitic	py	*58*			2635	7.39	188	1.10	7.71	4
	PacManus-RR	Basaltic–rhyolitic	cpy	*75*			470	23.5	84.5	0.32	4.84	4
	PacManus-RR	Basaltic–rhyolitic	sph	*52*			1664	3.57	1576	0.02	43.3	4
	PacManus-SM	Basaltic–rhyolitic	cc	*5*			749		304	0.69	4.16	4
	PacManus-SM	Basaltic–rhyolitic	cpy	*25*			15237	1.39	875	1.66	4.99	4
	PacManus-SM	Basaltic–rhyolitic	py	*5*			5390	5.97	29.4		8.16	4
	PacManus-SM	Basaltic–rhyolitic	sph	*6*			17269	9.42	167		2.45	4
		MORB			56	200	0.11	0.21	14×10^{-3}	4.9×10^{-3}	1.2×10^{-3}	7

* 1—this study; 2—Keith et al. (2016) [8]; 3—Wang et al. (2017) [15]; 4—Wohlgemuth-Ueberwasser et al. (2015) [13]; 5—Melekestseva et al. (2014) [46]; 6—Melekestseva et al. (2017) [47]; 7—Arevalo and McDonough (2010) [48] and references therein.

5.2. Controls on Trace Elements in Chalcopyrite

Chalcopyrite is commonly enriched in Co, Se, and Bi [7] and is the dominant sulfide phase in ultramafic-hosted SMS deposits [3]. Recently, several papers reported LA-ICP-MS-based trace element data of chalcopyrite from basaltic-, ultramafic-, and felsic-hosted SMS deposits worldwide (e.g., [13–15]). Wohlgemuth-Ueberwasser et al. (2015) [13] documented that Au, Sb, As, Se, and Te enrichments in chalcopyrite are mainly controlled by submicroscopic inclusions (e.g., As–Au–Sb–Pb sulfosalts and/or tetrahedrite–tennantite), which are often elevated as a function of fluid temperature.

Our analyses showed that Se (61.5–1283 ppm) and Te (2.6–110 ppm) were enriched in chalcopyrite from the Kairei vent field, with a strong positive correlation between these two elements (R^2 = 0.96). Both elements are likely incorporated into the chalcopyrite lattice at high temperatures, with high solubilities of Se and Te in reduced hydrothermal fluids of ~350 °C [10,49–51]. Similar enrichments of Te in chalcopyrite were described by Logatchev and Semyenov-2, with Te concentrations reaching 39.6 and 42.0 ppm, respectively (Table 3; [13,14]). However, the Te content of chalcopyrite in most other SMS deposits is typically low. LA-ICP-MS analyses of chalcopyrite from Wocan, Turtle Pits, and PacManus yielded an average Te concentration of around 1 ppm (Table 3; [13,15]). Compared to the basaltic-hosted Wocan field, chalcopyrite from Kairei was also shown to be highly enriched in Co, with a wide range of concentrations from 32.1 to 1781 ppm (Table 3; [15]), which could be derived from ultramafic rocks in the reaction zone. Maslennikov et al. (2009) [42] suggested that the Co enrichment in chalcopyrite from fossil vent chimneys in a volcanogenic-hosted massive sulfide deposit in the Southern Urals is related to Co-bearing mineral inclusions, such as cobaltite, arsenides, sulfoarsenides, and telluride. However, no positive correlation was observed between the concentrations of Co and Te/As in chalcopyrite from the Kairei vent field, and the pattern of the Co signal intensities correlated with Fe (Figure 3B, C), indicating that Co most likely substitutes for Fe. Antimony (<2.3 ppm) and As concentrations (<50.6 ppm) were relatively low in chalcopyrite from Kairei. These concentrations are similar to those described from other SMS deposits from mid-ocean ridge systems worldwide (Table 3). For example, a similar low concentration of Sb has been observed in chalcopyrite from Turtle Pits, Logatchev, Wocan, and Semyenov-2 (average usually <30 ppm). In contrast, Sb-rich chalcopyrite is common in back-arc basins and the enrichment there is thought to be mainly controlled by the occurrence of Sb-bearing mineral inclusions related to an increased flux of elements such as Sb due to the input of magmatic volatiles [13]. Most chalcopyrite from Kairei contains <0.2 ppm Au; however, single measurements with enrichments in Au (3.5 ppm, 2.3 ppm; Table S2) do occur and might indicate the occurrence of native gold inclusions (Figure 2F).

5.3. Controls on Trace Elements in Sphalerite

As one of the major sulfide minerals in the SMS deposits, sphalerite precipitates under a range of pressure, temperature, and fO_2-fS_2 conditions [52]. At Kairei, sphalerite from the Zn-rich chimneys was shown to be highly enriched in Cd, Pb, Co, As, Sn, Ga, Ge, Ag, and Sb compared to the other minerals. Cadmium, Co, Ga, and Sn showed clear positive correlations with an increasing temperature (Figure 7) calculated following the $Fe/Zn_{sphalerite}$ equation of Keith et al. (2014) [53]. In contrast, Ag, As, Ge, and Pb were characterized by negative correlations with temperature and precipitate as a consequence of an increasing fO_2 of the hydrothermal fluids due to significant mixing with seawater (Figure 7). Trace element concentrations in sphalerite showed strong positive correlations (Figure 8) for Pb–Ag (R^2 = 0.98), Pb–Au (R^2 = 0.83), Co–Cd (R^2 = 0.67), Cu–Sn (R^2 = 0.91), Ga–Sn (R^2 = 0.90), As–Ge (R^2 = 0.95), and Sb–Cd (R^2 = 0.79). The high concentrations of Cd (609–1792 ppm) and Co (196–993 ppm) were likely caused by the substitution of Zn^{2+} by Cd^{2+} and Co^{2+} (e.g., [52,54]). A high concentration of Pb (420–6396 ppm) accompanied by similarly high Ag concentrations (44–882 ppm) in sphalerite most likely indicates that the Ag occurs as Pb–Ag sulfosalts rather than as native silver associated with galena. The concentration of Au was generally low in sphalerite (<0.5 ppm); however, Au is related to Pb ($R^2_{Ag\text{-}Au}$ = 0.68), suggesting co-precipitation with Au as electrum inclusions in galena. The positive correlation between Sn and Cu, as well as between Sn and Ga, may be attributed

to the substitution of Zn^{2+} by Ga^{2+} or Ga^{3+} [12], or $3Zn^{2+}$ by Sn^{4+} + Cu^{2+} [52]. This substitution would also explain the Sn enrichment in bulk samples from Zn-rich chimneys (101–510 ppm; [4]). Sphalerite is also enriched in Ge and As with concentrations ranging from 72 ppm to 336 ppm and from 61 ppm to 502 ppm, respectively, which are similar to sphalerite from the Wocan hydrothermal field at the Carlsberg Ridge [15]. Although Ge^{4+} represents the more common oxidation state, Cook et al. (2009) [52] proposed a direct $Ge^{2+} \leftrightarrow Zn^{2+}$ substitution in sphalerite. The strong correlation of As with Ge (R^2 = 0.95) in sphalerite from Kairei suggests that both elements are enriched in sphalerite precipitating under medium temperature and moderately reduced conditions [52].

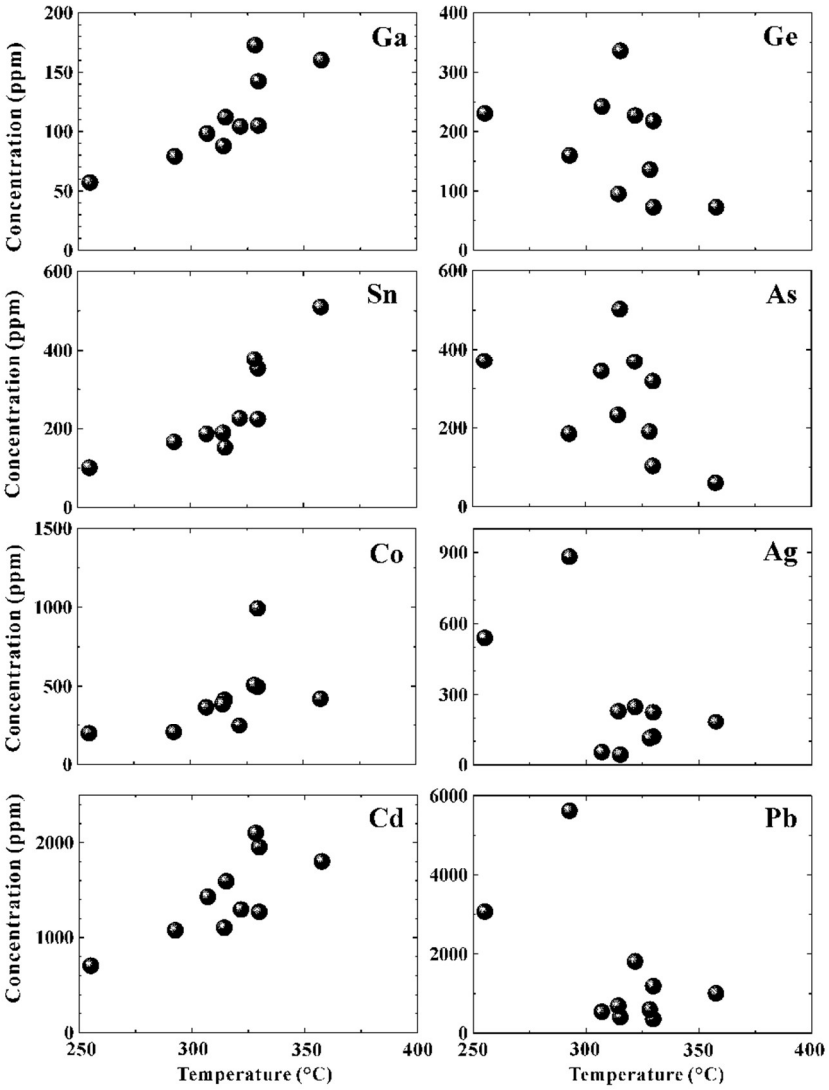

Figure 7. Correlation between the concentrations of trace elements in sphalerite and precipitation temperatures calculated from Keith et al. (2014) [53].

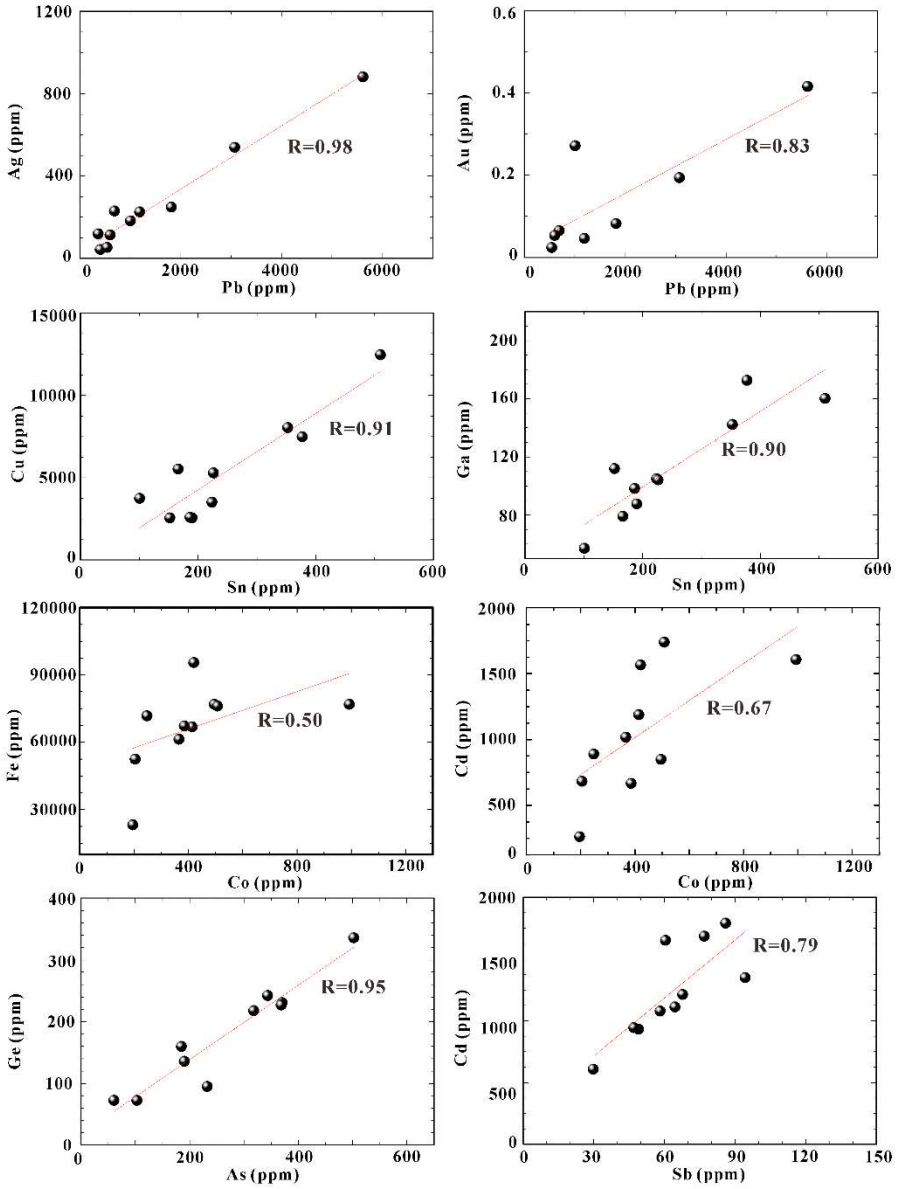

Figure 8. Trace element correlations of sphalerite for Pb–Ag, Pb–Au, Sn–Cu, Sn–Ga, Co–Fe, Co–Cd, As–Ge, and Sb–Cd from Zn-rich chimney samples.

5.4. Controls on Trace Elements in Bornite, Digenite, and Covellite

Bornite, digenite, and covellite are common Cu–(Fe)–sulfide minerals in SMS deposits which often precipitate under more oxidizing conditions caused by the ingress of seawater during the waning stages of hydrothermal activity (e.g., [3,4,51,55]). Due to the interaction of cooling hydrothermal fluids with cold, oxygenated seawater, U, V, and sometimes Ag may reach high concentrations in low temperature bornite and digenite formed during the latest hydrothermal phase or during secondary oxidation of primary sulfides (e.g., [14,15,47]). In contrast, bornite precipitated at higher temperatures has relatively high concentrations of Sn and In [15]. Additionally, Cook et al. (2011) [56] stated that high temperature primary bornite is an excellent host for Bi and Se. In our dataset, the highest Bi (up to 191 ppm) and Se (up to 2272 ppm) concentrations were found in bornite and may be explained by the incorporation of Bi into the bornite crystal lattice [56]. Cobalt concentrations in bornite–digenite were typically close to their respective minimum detection limits. However, in some spots, high Co concentrations (>1000 ppm; Figure 4) were observed, and based on the flat signal intensities of Co, we suppose this to represent local substitution of Co into the Fe site within bornite (Figure 3E).

5.5. Comparison with Mafic- and Ultramafic-Hosted SMS Deposits

The concentrations of trace elements in the ores from the SMSs, especially those that are mobilized at relatively low temperatures, are remarkably sensitive to the source rock concentrations in different tectonic settings (e.g., [3,7,57]). For example, mafic- and ultramafic-hosted SMSs at mid-ocean ridges are often enriched in Ni and Co [3,4,58], whereas felsic-hosted deposits in volcanic arc settings are enriched in Pb, As, Ag, Sb, and Sn [7]. Previous studies concluded that the presence of elevated Ni and Co concentrations in the sulfide minerals from ultramafic SMS deposits originates from the ultramafic substrate (1960 ppm Ni and 106 ppm Co in depleted mantle versus 104 ppm Ni and 44 ppm Co in MORB [59,60]). However, depositional conditions may also play significant roles in determining the final metal concentrations in the sulfide minerals [58].

Pyrite from ultramafic-hosted Kairei, Logatchev, and Semyenov-1 showed higher concentrations of Au (>1 ppm on average) than pyrite from the mafic-hosted Wocan, MESO, TAG, Turtle Pits, and MAR 5°S (Au <1 ppm) along the mid-ocean ridge (Table 3; Figure 9). Keith et al. (2016) [8] proposed that serpentinization in ultramafic-hosted vent systems plays an important role on Au enrichment in pyrite with low As contents. However, compared with felsic-hosted SMS deposits, sulfide minerals from the ultramafic-hosted deposits presented higher concentrations of Se and Te, but lower As, Sb, and Au concentrations (Table 3), which is most likely attributed to more reducing conditions at mid-ocean ridges and the contribution of magmatic volatiles in arc-related occurrences [13]. Significant variations of Ni/As versus Au/As ratios in pyrite were observed between ultramafic- and mafic-hosted SMS occurrences (Figure 9). This implies that there is an ultramafic influence on Au and Ni enrichment in pyrite from Kairei. However, the ultramafic-hosted Semyenov-1 showed lower Ni concentrations that were associated with higher Au and As concentrations (averages of 33.1 ppm Au and 510 ppm As; Table 3; Figure 9), Melekestseva et al. (2014) [46] suggested that a mafic substrate might contribute to those elements in the Semyenov-1. Clearly, investigations on the trace element behavior in other ultramafic-hosted sites, such as Rainbow, Ashadze and others, are needed to verify this observation.

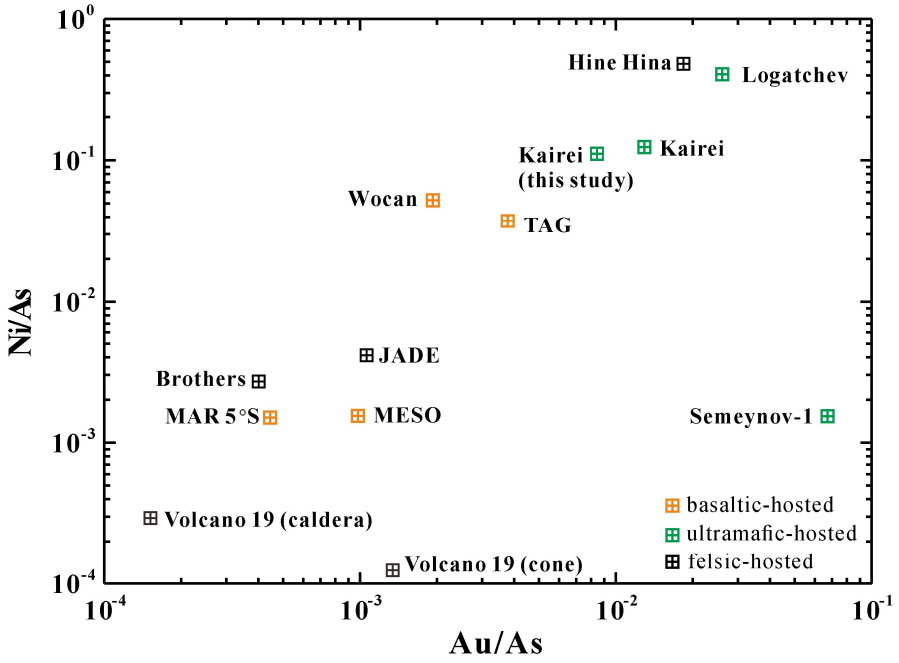

Figure 9. Variations of Ni/As vs. Au/As in pyrite from ultramafic- and mafic-hosted hydrothermal systems at mid-ocean ridges and felsic-hosted sites occurred in the back-arc basin/arc volcanoes. See the data source in Table 3.

To be able to compare the differences in trace element concentrations of chalcopyrite between ultramafic/mafic- and felsic-hosted deposits, we normalized the trace elements to global MORB [48]

(Figure 10). Chalcopyrite from Kairei showed a higher concentration of Se relative to Wocan, Semyenov-2, and Logatchev, but lower concentrations of As and Sb (Table 3; Figure 10). The general enrichment of Se in chalcopyrite is a factor of fluid temperature, with high solubility of Se in fluids of ~350 °C [10,49,61]. A host rock influence (mafic versus ultramafic) can probably be neglected since significant Se enrichment in chalcopyrite has been found in both, ultramafic- and mafic-hosted SMSs (e.g., average: ~2000 ppm, Broken Spur [62]).

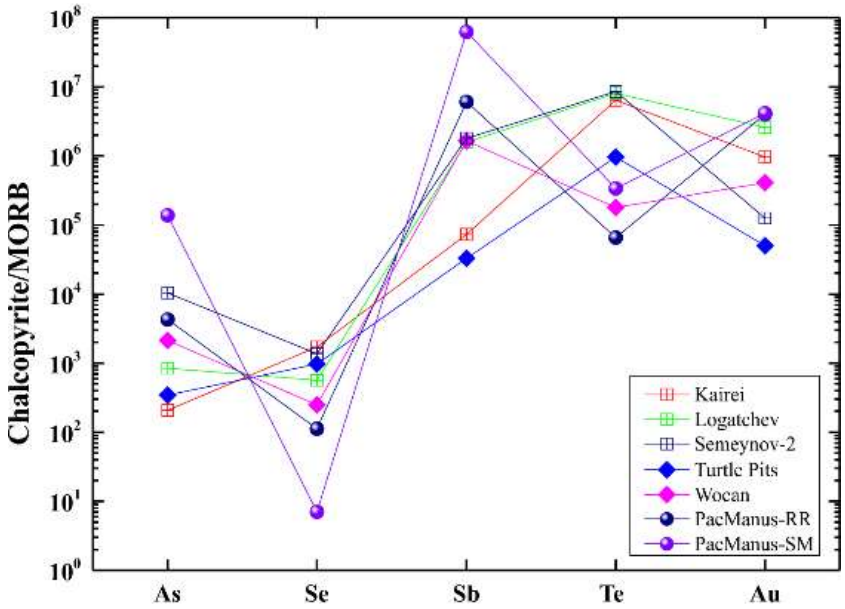

Figure 10. Selected MORB-normalized trace element patterns for chalcopyrite from different seafloor hydrothermal systems. MORB data source from Arevalo and McDonough (2010) [48].

Supplementary Materials: The following are available online at http://www.mdpi.com/2075-163X/8/11/526/s1, Table S1: LA-ICP-MS reference materials, Table S2: Trace and main element concentrations (ppm) of the analyzed sulfides at the Kairei vent field obtained from LA-ICP-MS and EPMA.

Author Contributions: Yejian Wang and Xiqiu Han conceived this contribution; Yejian Wang, Sven Petersen, and Xiqiu Han wrote the paper with contributions from Matthias Frische, Zhongyan Qiu, Yiyang Cai and Peng Zhou; Matthias Frische performed the LA-ICP-MS experiments, analyzed the data.

Funding: This study is funded by National Key Research and Development Program of China (2018YFC0309903), China Ocean Mineral Resources R&D Association project (DY135-S2-1-05), the Scientific Research Fund of the Second Institute of Oceanography, SOA (grant number QNYC1701) and Sino-German Cooperation Project on Marine and Polar Research (BMBF grant number 03F0724A).

Acknowledgments: We appreciate the great help from Dagmar Rau for her assistance with the LA-ICP-MS analyses. We also thank three anonymous referees for their valuable comments on an earlier version of this paper.

Conflicts of Interest: The authors declare no conflicts of interest.

References

1. Hannington, M.D.; de Ronde, C.D.; Petersen, S. Sea-floor tectonics and submarine hydrothermal systems. *Econ. Geol.* **2005**, *100*, 111–141.
2. Binns, R.A.; Scott, S.D. Actively forming polymetallic sulfide deposits associated with felsic volcanic rocks in the eastern Manus back-arc basin, Papua New Guinea. *Econ. Geol.* **1993**, *88*, 2226–2236. [CrossRef]
3. Fouquet, Y.; Pierre, C.; Etoubleau, J.; Charlou, J.L.; Ondréas, H.; Barriga, F.J.A.S.; Cherkashov, G.; Semkova, T.; Poroshina, I.; Bohn, M.; et al. Geodiversity of hydrothermal along the Mid-Atlantic Ridge and ultramafic-hosted mineralization: A new type of oceanic Cu-Zn-Co-Au Volcanogenic Massive Sulfide Deposit. In *Diversity of Hydrothermal Systems on Slow Spreading Ocean Ridges*; Rona, P.A., Devey, C.W., Dyment, J., Murton, B.J., Eds.; AGU: Washington, DC, USA, 2010; pp. 321–367.

4. Wang, Y.; Han, X.; Petersen, S.; Jin, X.; Qiu, Z.; Zhu, J. Mineralogy and geochemistry of hydrothermal precipitates from Kairei hydrothermal field, Central Indian Ridge. *Mar. Geol.* **2014**, *354*, 69–80. [CrossRef]
5. German, C.R.; Petersen, S.; Hannington, M.D. Hydrothermal exploration of mid-ocean ridges: Where might the largest sulfide deposits be forming? *Chem. Geol.* **2016**, *420*, 114–126. [CrossRef]
6. Monecke, T.; Petersen, S.; Hannington, M.D.; Grant, H.; Samson, I. The minor element endowment of modern sea-floor massive sulfides and comparison with deposits hosted in ancient volcanic successions. *Rev. Econ. Geol.* **2016**, *18*, 245–306.
7. Hannington, M.D. Volcanogenic Massive Sulfide Deposits. In *Treatise on Geochemistry*, 2nd ed.; Holland, H.D., Turekian, K.K., Eds.; Elsevier: Oxford, UK, 2014; pp. 463–488.
8. Keith, M.; Häckel, F.; Haase, K.M.; Schwarz-Schampera, U.; Klemd, R. Trace element systematics of pyrite from submarine hydrothermal vents. *Ore Geol. Rev.* **2016**, *72*, 728–745. [CrossRef]
9. Fontboté, L.; Kouzmanov, K.; Chiaradia, M.; Pokrovski, G.S. Sulfide Minerals in Hydrothermal Deposits. *Elements* **2017**, *13*, 97–103. [CrossRef]
10. Butler, I.B.; Nesbitt, R.W. Trace element distributions in the chalcopyrite wall of a black smoker chimney: insights from laser ablation inductively coupled plasma mass spectrometry (LA-ICP-MS). *Earth Planet. Sci. Lett.* **1999**, *167*, 335–345. [CrossRef]
11. Lein, A.; Bogdanov, Y.; Maslennikov, V.; Li, S.; Ulyanova, N.; Maslennikova, S.; Ulyanov, A. Sulfide minerals in the Menez Gwen nonmetallic hydrothermal field (Mid-Atlantic Ridge). *Lithol. Miner. Resour.* **2010**, *45*, 305–323. [CrossRef]
12. Ye, L.; Cook, N.J.; Ciobanu, C.L.; Yuping, L.; Qian, Z.; Tiegeng, L.; Wei, G.; Yulong, Y.; Danyushevsky, L.V. Trace and minor elements in sphalerite from base metal deposits in South China: A LA-ICPMS study. *Ore Geol. Rev.* **2011**, *39*, 188–217. [CrossRef]
13. Wohlgemuth-Ueberwasser, C.C.; Viljoen, F.; Petersen, S.; Vorster, C. Distribution and solubility limits of trace elements in hydrothermal black smoker sulfides: An in-situ LA-ICP-MS study. *Geochim. Cosmochim. Acta* **2015**, *159*, 16–41. [CrossRef]
14. Melekestseva, I.Y.; Maslennikov, V.V.; Tret'Yakov, G.A.; Nimis, P.; Beltenev, V.E.; Rozhdestvenskaya, I.I.; Maslennikova, S.P.; Belogub, E.V.; Danyushevsky, L.V.; Large, R.R.; et al. Gold- and Silver-Rich Massive Sulfides from the Semenov-2 Hydrothermal Field, 13°31.13′N, Mid-Atlantic Ridge: A Case of Magmatic Contribution? *Econ. Geol.* **2017**, *112*, 741–773. [CrossRef]
15. Wang, Y.; Han, X.; Petersen, S.; Frische, M.; Qiu, Z.; Li, H.; Li, H.; Wu, Z.; Cui, R. Mineralogy and trace element geochemistry of sulfide minerals from the Wocan Hydrothermal Field on the slow-spreading Carlsberg Ridge, Indian Ocean. *Ore Geol. Rev.* **2017**, *84*, 1–19. [CrossRef]
16. Gamo, T.; Chiba, H.; Yamanaka, T.; Okudaira, T.; Hashimoto, J.; Tsuchida, S.; Ishibashi, J.; Kataoka, S.; Tsunogai, U.; Okamura, K.; et al. Chemical characteristics of newly discovered black smoker fluids and associated hydrothermal plumes at the Rodriguez Triple Junction, Central Indian Ridge. *Earth Planet. Sci. Lett.* **2001**, *193*, 371–379. [CrossRef]
17. Van Dover, C.L.; Humphris, S.E.; Fornari, D.; Cavanaugh, C.M.; Collier, R.; Goffredi, S.K.; Hashimoto, J.; Lilley, M.D.; Reysenbach, A.L.; Shank, T.M.; et al. Biogeography and ecological setting of Indian Ocean hydrothermal vents. *Science* **2001**, *294*, 818–823. [CrossRef] [PubMed]
18. Kumagai, H.; Nakamura, K.; Toki, T.; Morishita, T.; Okino, K.; Ishibashi, J.; Tsunogai, U.; Kawaguacci, S.; Gamo, T.; Shibuya, T.; et al. Geological background of the Kairei and Edmond hydrothermal fields along the Central Indian Ridge: Implications of their vent fluids' distinct chemistry. *Geofluids* **2008**, *8*, 239–251. [CrossRef]
19. Gallant, R.M.; Von Damm, K.L. Geochemical controls on hydrothermal fluids from the Kairei and Edmond Vent Fields, 23°–25° S, Central Indian Ridge. *Geochem. Geophys. Geosyst.* **2006**, *7*, Q6018. [CrossRef]
20. Kelley, D.S.; Karson, J.A.; Blackman, D.K.; Fruh-Green, G.L.; Butterfield, D.A.; Lilley, M.D.; Olson, E.J.; Schrenk, M.O.; Roe, K.K.; Lebon, G.T.; et al. An off-axis hydrothermal vent field near the Mid-Atlantic Ridge at 30°N. *Nature* **2001**, *412*, 145–149. [CrossRef] [PubMed]
21. Douville, E.; Charlou, J.L.; Oelkers, E.H.; Bienvenu, P.; Jove Colon, C.F.; Donval, J.P.; Fouquet, Y.; Prieur, D.; Appriou, P. The rainbow vent fluids (36°14′N, MAR): The influence of ultramafic rocks and phase separation on trace metal content in Mid-Atlantic Ridge hydrothermal fluids. *Chem. Geol.* **2002**, *184*, 37–48. [CrossRef]

22. Charlou, J.L.; Donval, J.P.; Fouquet, Y.; Jean-Baptiste, P.; Holm, N. Geochemistry of high H_2 and CH_4 vent fluids issuing from ultramafic rocks at the Rainbow hydrothermal field (36°14′ N, MAR). *Chem. Geol.* **2002**, *191*, 345–359. [CrossRef]
23. Charlou, J.L.; Donval, J.P.; Konn, C.; Ondréas, H.; Fouquet, Y. High production and fluxes of H_2 and CH_4 and evidence of abiotic hydrocarbon synthesis by serpentinization in ultramafic-hosted hydrothermal systems on the Mid-Atlantic Ridge. In *Diversity of Hydrothermal Systems on Slow Spreading Ocean Ridges*; Rona, P.A., Devey, C.W., Dyment, J., Murton, B.J., Eds.; AGU: Washington, DC, USA, 2010; pp. 265–296.
24. Melchert, B.; Devey, C.W.; German, C.R.; Lackschewitz, K.S.; Seifert, R.; Walter, M.; Mertens, C.; Yoerger, D.R.; Baker, E.T.; Paulick, H.; et al. First evidence for high-temperature off-axis venting of deep crustal/mantle heat: The Nibelungen hydrothermal field, southern Mid-Atlantic Ridge. *Earth Planet. Sci. Lett.* **2008**, *275*, 61–69. [CrossRef]
25. Nakamura, K.; Morishita, T.; Bach, W.; Klein, F.; Hara, K.; Okino, K.; Takai, K.; Kumagai, H. Serpentinized troctolites exposed near the Kairei Hydrothermal Field, Central Indian Ridge: Insights into the origin of the Kairei hydrothermal fluid supporting a unique microbial ecosystem. *Earth Planet. Sci. Lett.* **2009**, *280*, 128–136. [CrossRef]
26. Fujii, M.; Okino, K.; Sato, T.; Sato, H.; Nakamura, K. Origin of magnetic highs at ultramafic hosted hydrothermal systems: Insights from the Yokoniwa site of Central Indian Ridge. *Earth Planet. Sci. Lett.* **2016**, *441*, 26–37. [CrossRef]
27. Morishita, T.; Hara, K.; Nakamura, K.; Sawaguchi, T.; Tamura, A.; Arai, S.; Okino, K.; Takai, K.; Kumagai, H. Igneous, alteration and exhumation processes recorded in abyssal peridotites and related fault rocks from an oceanic core complex along the Central Indian Ridge. *J. Petrol.* **2009**, *50*, 1299–1325. [CrossRef]
28. Okino, K.; Nakamura, K.; Sato, H. Tectonic background of four hydrothermal fields along the Central Indian Ridge. In *Subseafloor Biosphere Linked to Hydrothermal Systems: TAIGA Concept*; Ishibashi, J., Okino, K., Sunamura, M., Eds.; Springer Japan: Tokyo, Japan, 2015; pp. 133–146.
29. Ryan, W.B.F.; Carbotte, S.M.; Coplan, J.O.; O'Hara, S.; Melkonian, A.; Arko, R.; Weissel, R.A.; Ferrini, V.; Goodwillie, A.; Nitsche, F.; et al. Global Multi-Resolution Topography synthesis. *Geochem. Geophys. Geosyst.* **2009**, *10*, Q03014. [CrossRef]
30. Wang, Y.; Han, X.; Jin, X.; Qiu, Z.; Ma, Z.; Yang, H. Hydrothermal activity events at Kairei Field, Central Indian Ridge 25° S. *Resour. Geol.* **2012**, *62*, 208–214. [CrossRef]
31. Wise, S.; Watters, R. *Certificate of Analysis, Standard Reference Material 610*; National Institute of Standards and Technology (NIST): Gaithersburg, MD, USA, 2012.
32. Wohlgemuth-Ueberwasser, C.C.; McClung, C.R.; Viljoen, F. Metamorphic alteration of the massive sulfide horizon from the Salt River VMS deposit (South Africa). *Ore Geol. Rev.* **2014**, *56*, 45–52. [CrossRef]
33. Jochum, K.P.; Stoll, B.; Herwig, K.; Willbold, M.; Hofmann, A.W.; Amini, M.; Aarburg, S.; Abouchami, W.; Hellebrand, E.; Mocek, B.; et al. MPI-DING reference glasses for in situ microanalysis: New reference values for element concentrations and isotope ratios. *Geochem. Geophys. Geosyst.* **2006**, *7*, Q02008. [CrossRef]
34. Fietzke, J.; Frische, M. Experimental evaluation of elemental behavior during LA-ICP-MS: influences of plasma conditions and limits of plasma robustness. *J. Anal. At Spectrom.* **2016**, *31*, 234–244. [CrossRef]
35. Fietzke, J.; Liebetrau, V.; Guenther, D.; Guers, K.; Hametner, K.; Zumholz, K.; Hansteen, T.H.; Eisenhauer, A. An alternative data acquisition and evaluation strategy for improved isotope ratio precision using LA-MC-ICP-MS applied to stable and radiogenic strontium isotopes in carbonates. *J. Anal. At. Spectrom.* **2008**, *23*, 955–961. [CrossRef]
36. Tivey, M.K.; Humphris, S.E.; Thompson, G.; Hannington, M.D.; Rona, P.A. Deducing patterns of fluid flow and mixing within the TAG active hydrothermal mound using mineralogical and geochemical data. *J. Geophys. Res.* **1995**, *100*, 12527–12555. [CrossRef]
37. Herzig, P.M.; Hannington, M.D.; Arribas, A., Jr. Sulfur isotopic composition of hydrothermal precipitates from the Lau back-arc: implications for magmatic contributions to seafloor hydrothermal systems. *Miner. Depos.* **1998**, *33*, 226–237. [CrossRef]
38. De Ronde, C.; Massoth, G.; Butterfield, D.; Christenson, B.; Ishibashi, J.; Ditchburn, R.; Hannington, M.; Brathwaite, R.; Lupton, J.; Kamenetsky, V.; et al. Submarine hydrothermal activity and gold-rich mineralization at Brothers Volcano, Kermadec Arc, New Zealand. *Miner. Depos.* **2011**, *46*, 541–584. [CrossRef]
39. Vaughan, D.J.; Rosso, K.M. Chemical bonding in sulfide minerals. *Rev. Miner. Geochem.* **2006**, *61*, 231–264. [CrossRef]

40. Chouinard, A.; Paquette, J.; Williams-Jones, A.E. Crystallographic controls on trace-element incorporation in auriferous pyrite from the Pascua epithermal high-sulfidation deposit, Chile-Argentina. *Can. Mineral.* **2005**, *43*, 951–963. [CrossRef]
41. Blanchard, M.; Alfredsson, M.; Brodholt, J.P.; Wright, K.; Catlow, C.R.A. Arsenic incorporation into FeS_2 pyrite and its influence on dissolution: A DFT study. *Geochim. Cosmochim. Acta* **2007**, *71*, 624–630. [CrossRef]
42. Maslennikov, V.V.; Maslennikova, S.P.; Large, R.R.; Danyushevsky, L.V. Study of trace element zonation in vent chimneys from the Silurian Yaman-Kasy volcanic-hosted massive sulfide deposit (Southern Urals, Russia) using laser ablation-inductively coupled plasma mass spectrometry (LA-ICPMS). *Econ. Geol.* **2009**, *104*, 1111–1141. [CrossRef]
43. Revan, M.K.; Genç, Y.; Maslennikov, V.V.; Maslennikova, S.P.; Large, R.R.; Danyushevsky, L.V. Mineralogy and trace-element geochemistry of sulfide minerals in hydrothermal chimneys from the Upper-Cretaceous VMS deposits of the eastern Pontide orogenic belt (NE Turkey). *Ore Geol. Rev.* **2014**, *63*, 129–149. [CrossRef]
44. Schmidt, K.; Koschinsky, A.; Garbe-Schönberg, D.; De Carvalho, L.M.; Seifert, R. Geochemistry of hydrothermal fluids from the ultramafic-hosted Logatchev hydrothermal field, 15°N on the Mid-Atlantic Ridge: Temporal and spatial investigation. *Chem. Geol.* **2007**, *242*, 1–21. [CrossRef]
45. Seyfried, W.E.; Ding, K. Phase equilibria in subseafloor hydrothermal systems: A review of the role of redox, temperature, pH and dissolved Cl on the chemistry of hot spring fluids at Mid-Ocean Ridges. In *Seafloor Hydrothermal Systems, Physical, Chemical, Biological, and Geological Interactions*; Humphris, S.R., Zierenberg, R.A., Mullineaux, L.S., Thomson, R.E., Eds.; AGU: Washington, DC, USA, 1995; pp. 248–272.
46. Melekestseva, I.Y.; Tret'Yakov, G.A.; Nimis, P.; Yuminov, A.M.; Maslennikov, V.V.; Maslennikova, S.P.; Kotlyarov, V.A.; Beltenev, V.E.; Danyushevsky, L.V.; Large, R.R. Barite-rich massive sulfides from the Semenov-1 hydrothermal field (Mid-Atlantic Ridge, 13°30.87′ N): Evidence for phase separation and magmatic input. *Mar. Geol.* **2014**, *349*, 37–54. [CrossRef]
47. Melekestseva, I.Y.; Maslennikov, V.V.; Maslennikova, S.P.; Danyushevsky, L.V.; Large, R. Covellite of the Semenov-2 hydrothermal field (13°31.13′ N, Mid-Atlantic Ridge): Enrichment in trace elements according to LA ICP MS analysis. *Dokl. Earth Sci.* **2017**, *473*, 291–295. [CrossRef]
48. Arevalo, R.; McDonough, W.F. Chemical variations and regional diversity observed in MORB. *Chem. Geol.* **2010**, *271*, 70–85. [CrossRef]
49. Auclair, G.; Fouquet, Y.; Bohn, M. Distribution of selenium in high-temperature hydrothermal sulfide deposits at 13° North, East Pacific Rise. *Can. Mineral.* **1987**, *25*, 577–587.
50. Hannington, M.D.; Herzig, P.M.; Scott, S.D.; Thompson, G.; Rona, P.A. Comparative mineralogy and geochemistry of gold-bearing sulfide deposits on the mid-ocean ridges. *Mar. Geol.* **1991**, *101*, 217–248. [CrossRef]
51. Halbach, P.; Fouquet, Y.; Herzig, P. Mineralization and compositional patterns in deep-sea hydrothermal systems. In *Energy and mass transfer in marine hydrothermal systems*; Tunnicliffe, V., Hein, J.R., Eds.; Dahlem University Press: Berlin, Germany, 2003; pp. 85–122.
52. Cook, N.J.; Ciobanu, C.L.; Mao, J. Textural control on gold distribution in As-free pyrite from the Dongping, Huangtuliang and Hougou gold deposits, North China Craton (Hebei Province, China). *Chem. Geol.* **2009**, *264*, 101–121. [CrossRef]
53. Keith, M.; Haase, K.M.; Schwarz-Schampera, U.; Klemd, R.; Petersen, S.; Bach, W. Effects of temperature, sulfur, and oxygen fugacity on the composition of sphalerite from submarine hydrothermal vents. *Geology* **2014**, *42*, 699–702. [CrossRef]
54. Rosso, K.M.; Vaughan, D.J. Sulfide Mineral Surfaces. *Rev. Miner. Geochem.* **2006**, *61*, 505–556. [CrossRef]
55. Mozgova, N.N.; Trubkin, N.V.; Borodaev, Y.S.; Cherkashev, G.A.; Stepanova, T.V.; Semkova, T.A.; Uspenskaya, T.Y. Mineralogy of massive sulfides from the Ashadze hydrothermal field, 13°N, Mid-Atlantic Ridge. *Can. Mineral.* **2008**, *46*, 545–567. [CrossRef]
56. Cook, N.J.; Ciobanu, C.L.; Danyushevsky, L.V.; Gilbert, S. Minor and trace elements in bornite and associated Cu–(Fe)-sulfides: A LA-ICP-MS study Bornite mineral chemistry. *Geochim. Cosmochim. Acta* **2011**, *75*, 6473–6496. [CrossRef]
57. Houghton, J.L.; Shanks, W.C., III; Seyfried, W.E., Jr. Massive sulfide deposition and trace element remobilization in the Middle Valley sediment-hosted hydrothermal system, northern Juan de Fuca Ridge. *Geochim. Cosmochim. Acta* **2004**, *68*, 2863–2873. [CrossRef]

58. Melekestseva, I.Y.; Zaykov, V.V.; Nimis, P.; Tret'Yakov, G.A.; Tessalina, S.G. Cu–(Ni–Co–Au)-bearing massive sulfide deposits associated with mafic–ultramafic rocks of the Main Urals Fault, South Urals: Geological structures, ore textural and mineralogical features, comparison with modern analogs. *Ore Geol. Rev.* **2013**, *52*, 18–36. [CrossRef]
59. Salters, V.J.M.; Stracke, A. Composition of the depleted mantle. *Geochem. Geophys. Geosyst.* **2004**, *5*, Q5B–Q7B. [CrossRef]
60. White, W.M.; Klein, E.M. Composition of the Oceanic Crust. In *Treatise on Geochemistry*, 2nd ed.; Holland, H.D., Turekian, K.K., Eds.; Elsevier: Oxford, UK, 2014; pp. 457–496.
61. Hannington, M.D.; Tivey, M.K.; Larocque, A.C.L.; Petersen, S.; Rona, P.A. The occurrence of gold in sulfide deposits of the TAG hydrothermal field, Mid-Atlantic Ridge. *Can. Mineral.* **1995**, *33*, 1285–1310.
62. Bogdanov, Y.A.; Lein, A.; Maslennikov, V.; Li, S.; Ul'yanov, A. Mineralogical-geochemical features of sulfide ores from the Broken Spur hydrothermal vent field. *Oceanology* **2008**, *48*, 679–700. [CrossRef]